



Research paper

Sensitivity of cartilage mechanical behaviour to spatial variations in material properties

Jonathan P. Whiteley^{a,*}, Cameron P. Brown^b, Eamonn A. Gaffney^c^a Department of Computer Science, University of Oxford, Parks Road, OX1 3QD, Oxford, United Kingdom^b MMPE, MERF, Faculty of Engineering, Queensland University of Technology, QLD 4000, Brisbane, Australia^c Mathematical Institute, University of Oxford, Andrew Wiles Building, Woodstock Road, OX2 6GG, Oxford, United Kingdom

ARTICLE INFO

Keywords:

Cartilage

Static loading

Dynamic loading

Sensitivity analysis

Material properties

ABSTRACT

Articular cartilage tissue exhibits a spatial dependence in material properties that govern mechanical behaviour. A mathematical model of cartilage tissue under one dimensional confined compression testing is developed for normal tissue that takes account of these variations in material properties. Modifications to the model representative of a selection of mechanisms driving osteoarthritic cartilage are proposed, allowing application of the model to both physiological and pathophysiological, osteoarthritic tissue. Incorporating spatial variations into the model requires the specification of more parameters than are required in the absence of these variations. A global sensitivity analysis of these parameters is implemented to identify the dominant mechanisms of mechanical response, in normal and osteoarthritic cartilage tissue, to both static and dynamic loading. The most sensitive parameters differ between dynamic and static mechanics of the cartilage, and also differ between physiological and osteoarthritic pathophysiological cartilage. As a consequence changes in cartilage mechanics in response to alterations in cartilage structure are predicted to be contingent on the nature of loading and the health, or otherwise, of the cartilage. In particular the mechanical response of cartilage, especially deformation, is predicted to be much more sensitive to cartilage stiffness in the superficial zone given the onset of osteoarthritic changes to material properties, such as superficial zone increases in permeability and reductions in fixed charge. In turn this indicates that any degenerative changes in the stiffness associated with the superficial cartilage collagen mesh are amplified if other elements of osteoarthritic disease are present, which provides a suggested mechanism-based explanation for observations that the range of mechanical parameters representative of normal and osteoarthritic tissue can overlap substantially.

1. Introduction

Effortless joint movement is predicated on the articulation of opposing bone surfaces with exceptionally low friction and lifetime longevity, despite frequent and extreme physiological loading. The exceptional tribological properties required for movement characterise the mechanical performance of the articular cartilage coating opposing bone in a joint. In turn, these properties emerge from the complex microstructure of cartilage, as extensively reported (Athanasίου et al., 2013; Klika et al., 2016; Mow et al., 1992).

In brief, articular cartilage tissue – also referred to as simply cartilage below – predominantly comprises interwoven type II collagen and proteoglycans immersed in interstitial fluid. The proteoglycans are mainly aggrecans with a side chain structure of negatively charged glycoaminoglycans. This fixed charge on the glycoaminoglycans generates a swelling pressure in the interstitial fluid, causing the articular cartilage to expand in size. This swelling allows cartilage to withstand large

loads, and aids the lubrication of shearing bone movement. Cartilage exhibits an extensive depth dependence in its structure on passing from the superficial zone of cartilage interfacing with the synovial fluid, through the middle and the deep zones, to the thin calcified zone that lies at the interface of cartilage with the underlying bone. For instance the orientation of the collagen transitions via the Benninghoff arcades (Benninghoff, 1925) from a perpendicular orientation relative to the bone interface in the calcified and deep zones, to a parallel orientation in the superficial zone (Buckwalter et al., 1994).

Furthermore, as will be our focus in this study, mechanical properties (Antons et al., 2018; Chen et al., 2001; Schinagl et al., 1997), proteoglycan density (Nieminen et al., 2002), permeability (Maroudas, 1968; Maroudas and Bullough, 1968) and fixed charge density (Chen et al., 2001) of cartilage change substantially with depth. The latter can be readily observed for fixed charge, as illustrated for normal, physiological cartilage in Fig. 1A, where red represents regions possessing

* Corresponding author.

E-mail addresses: jonathan.whiteley@cs.ox.ac.uk (J.P. Whiteley), cp.brown@qut.edu.au (C.P. Brown), gaffney@maths.ox.ac.uk (E.A. Gaffney).<https://doi.org/10.1016/j.jmbbm.2024.106575>

Received 25 September 2023; Received in revised form 28 February 2024; Accepted 8 May 2024

Available online 13 May 2024

1751-6161/© 2024 The Authors. Published by Elsevier Ltd. This is an open access article under the CC BY license (<http://creativecommons.org/licenses/by/4.0/>).

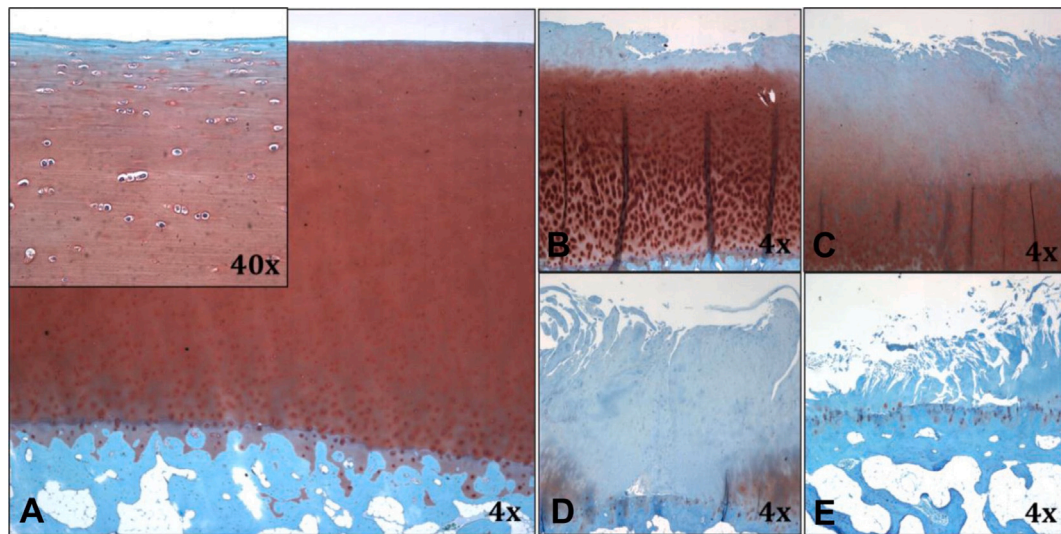


Fig. 1. Histological appearance of human cartilage with increasing osteoarthritic severity, showing progressive loss of fixed charge density and surface disruption. Sections stained by Safranin O-fast green, where red denotes high charge density magnitude and blue provides tissue contrast, denoting essentially zero fixed charge. Plot A illustrates normal, physiological tissue. The blue region at the bottom of this plot is bone. Plots B, C, D, E represent osteoarthritic pathophysiology of increasing severity, based on Mankin scores of 1–4, respectively; see [Mankin et al. \(1971\)](#) for a discussion of the Mankin system of grading cartilage degradation due to osteoarthritis. Note that the blue layer below the calcified layer of cartilage in plot A that represents bone does not always appear in plots B–E. Comparing plot B with plot A we see that there is a thicker blue layer in the superficial layer at the top of cartilage in plot B, corresponding to a loss of fixed charge in the superficial layer for mild osteoarthritis with Mankin score 1. In plot C, representing osteoarthritic degradation with Mankin score 2, the loss of fixed charge has progressed from the superficial layer into deeper cartilage layers. The loss of fixed charge then extends into almost the whole cartilage in plots D and E, representative of Mankin scores of 3 and 4. In this study we are concerned with modelling normal tissue and tissue with relatively mild osteoarthritis, i.e. tissue illustrated in plots A–C.

Source: Reproduced from [Pauli et al. \(2012\)](#).

a large negative fixed charge density and blue represents approximately neutral fixed charge density, noting the blue region at the base constitutes bone. Thus one can observe in normal cartilage that charge density is retained until very near to the cartilage interface with synovial fluid, as further illustrated by the sub-figure within [Fig. 1A](#). In addition the heterogeneous structure of cartilage and its fixed charge distribution is altered by osteoarthritis, as illustrated in [Fig. 1B–E](#), which respectively represent osteoarthritic disease of increasing severity. In particular the surface is increasingly rough, fragmented and worn away, with an inexorable loss of fixed charge initiating with the more superficial regions. This is caused by the loss of proteoglycans and manifests in subjects through a disruption in the load carrying capability ([Setton et al., 1993](#)), while the disruption of the cartilage surface with lost or decreased proteoglycan is associated with increased permeability ([Maroudas and Bullough, 1968](#); [Setton et al., 1993](#)).

Similarly, variation in the mechanical stiffness of cartilage with depth may be inferred from the variation in the confined compression modulus presented in [Fig. 2A](#), from the work of [Schinagl et al. \(1997\)](#). We observe an extensive increase in stiffness on moving from superficial layers of cartilage into deep cartilage. Analogous observations can be seen in measurements of diseased human cartilage, reproduced from [Antons et al. \(2018\)](#) in [Fig. 2B](#). More generally, extensive population variation is also regularly observed, for instance in normal and enzymatically treated cartilage for human specimens ([Brown et al., 2007](#)), as well as osteoarthritis ([Brown et al., 2007](#)), which is further highlighted for human pathology in [Fig. 2B](#).

Such variation highlights that modelling studies should not only consider depth dependence but also distributions of parameters, rather than point-parameter estimates. Furthermore, comparing and contrasting the mechanical properties of human cartilage for normal and osteoarthritic samples not only reveals substantial differences, but also that the qualitative mechanical characteristics are nonetheless preserved and the population distribution of many mechanical parameters overlap ([Brown et al., 2007](#)). In turn, this suggests that effectively the same mechanical model, albeit with different parameters, may be used to represent normal and osteoarthritic cartilage, with relatively little change. Despite difficulties in the reproducibility of in-vitro

enzymatically-induced proteoglycan degradation ([Moody et al., 2006](#)) and concomitant fixed charge loss and permeability increases, such enzymatic studies are still informative. In particular, the observation that qualitative mechanical characteristics are preserved on trypsin treatment even if detailed responses change ([Brown et al., 2007](#)), also suggests that representing the mechanics of cartilage with altered proteoglycan density, together with fixed charge and permeability changes, can once more be captured by parameter changes within the same mechanical modelling framework.

In addition, osteoarthritis may be initiated and progressed through any number of mechanisms, such as the stiffness and stiffness gradients of the underlying subchondral bone ([Hayami et al., 2006](#); [Radin and Rose, 1986](#)), or vascularisation or abnormal bone remodelling ([Kuyinu et al., 2016](#)). While such features cannot be captured in the modelling presented below, other mechanisms can be represented, such as the impact of increases in permeability, and fixed charge loss, which especially occur in the more superficial regions and are associated with cartilage surface disruption ([Saarakkala et al., 2010](#); [Setton et al., 1993](#)). However, the relationships between any of these latter features and mechanical performance in disease progression remains a challenge to characterise. In turn, this presents the difficulty that there are essentially no constraints beyond broad upper and lower bounds within the physiological range of possible parameters to enable a simplifying reduction in the dimensionality of a large parameter space in modelling studies, especially once cartilage depth dependence is considered.

Thus, an initial aim in this study is the development of a mathematical model of cartilage tissue that includes the physiological and osteoarthritic features described above, and is also amenable to methods of studying model response within a high dimensional parameter space. To enable this, we extend a poroviscoelastic model that includes electrochemical swelling ([Whiteley and Gaffney, 2020](#)) to include spatial inhomogeneities representative of both normal, physiological cartilage and osteoarthritic pathophysiology. Hence the model is at the tissue level, but with nano-scale properties, such as fixed charge induced swelling, systematically incorporated into the tissue level description, so that fixed charge effects are explicitly considered at the macroscale.

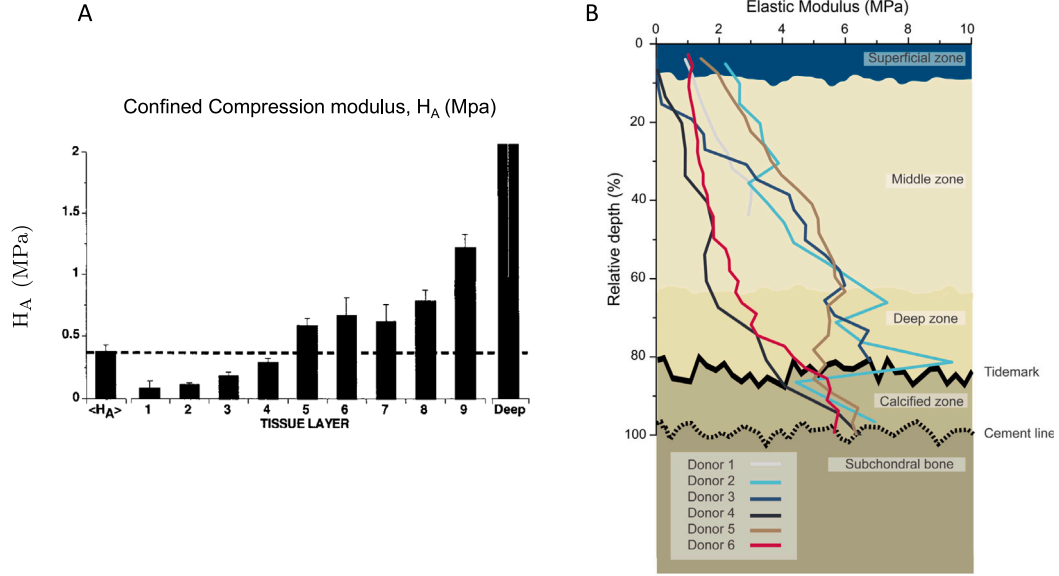


Fig. 2. The variation in stiffness of cartilage with depth. Left (A). The confined compression modulus H_A denotes the stiffness modulus for a material where lateral movement is constrained in compression and is presented for bovine patello-femoral groove cartilage. Each of the tissue layers labelled 1–9 represent layers of tissue of thickness 125 μm , with tissue layer 1 the superficial layer and subsequent tissue layers progressively deeper into the cartilage. Deep tissue represents all tissue deeper than tissue layer 9. The layers of tissue exhibit increasing stiffness, from superficial to deep layers. The small bars denote the standard error of mean ($n = 6$). Right (B) The elastic modulus, determined from the indentation technique described by Antons et al. (2018), for diseased human cartilage from $n = 6$ donors. Donors 1–4 presented with Collins grade II osteoarthritis, i.e. moderate cartilage degradation due to osteoarthritis, and donors 5 and 6 presented with osteochondritis dissecans; see Collins (1939, 1949) for a discussion of the Collins system of grading osteoarthritis. Note the depth variation and the wide spread between individual donors. Plot (A) has been reproduced from Schinagl et al. (1997) and plot (B) has been reproduced from Antons et al. (2018).

There are numerous other mathematical models of cartilage tissue in the literature, each with their specific focus, as reviewed for example by the commentaries (Ateghian, 2007; Klika et al., 2016; Mohammadi et al., 2013; Pierce, 2022), with references therein. The main distinction between the model used in this study and other tissue level models of cartilage tissue is that the model used in this study includes a swelling term that has been rationally derived taking account of the underlying coupling of electrochemistry and mechanics at the nanoscale. Thus, while this model will inevitably possess a high dimensional parameter space due to the parameterisation of depth dependence, the upscaling to the tissue level will nonetheless allow both the systematic accommodation of nanoscale swelling mechanics and sufficiently efficient simulation for the examination of model behaviour globally across parameter space. Thus, our primary aim will be to conduct global sensitivity analyses to identify the parameters – and thus the associated cartilage properties and their depth variation – that are predicted to predominantly drive major features of tissue scale mechanical response in normal tissue and osteoarthritic pathophysiology.

We will use the model to predict the mechanics of the confined compression experiment described in, for example, DiSilvestro and Suh (2001). This experiment is typically performed using a sample that is initially deformed due to swelling and is of length L_{swell} . A permeable plunger then compresses the sample to a length of $0.9L_{\text{swell}}$, and the sample is held at this deformed length until the reaction force on the plunger reaches a constant value. The sample is then compressed further to $0.85L_{\text{swell}}$ over a period of 50 s, and subsequently held at this deformed length. A schematic diagram illustrating the confined compression experiment is shown in Fig. 3(a), where the distance $d(t)$ is the height of the plunger at time t and is set by the experiment. The output from the experiment is the force on the plunger as a function of time; an exemplar output plot is given in Fig. 3(b). In particular, the sensitivity analysis will be used to identify fundamental features of cartilage tissue and its depth heterogeneity that predominantly affect the mechanical response of cartilage to both static and dynamic confined compression loading, and whether these responses are predicted to differ between normal and osteoarthritic cartilage.

The remainder of this paper is structured as follows. We begin by presenting the equations describing cartilage deformation for the cartilage compression experiment in Section 2. In Section 3 we specify spatial variations in material properties that encapsulate the features discussed above, for both normal and osteoarthritic cartilage, and justify our choices of constitutive relations. This section is concluded with an example of parameters choices where the model is not suitable to describe the compression loading experiment, together with an explanation of why this is the case. Noting this excludes many methods of global sensitivity analysis, but not principal component based analysis (Jolliffe and Cadima, 2016), the latter is implemented in Section 4, with an evaluation and discussion of the results in Section 5.

2. The governing equations

We model the compression of a one-dimensional cartilage sample of undeformed length L discussed in Section 1, and assume that cartilage tissue may be modelled as a poroviscoelastic material subject to swelling due to charges on the solid scaffold. Deformations are described by Whiteley and Gaffney (2020):

$$\frac{\partial}{\partial X} \left(S - \theta_{s,0} \left(\frac{\partial x}{\partial X} \right)^{-1} \frac{Q_s^2}{\epsilon_f} - p \right) = 0, \quad (1)$$

$$\frac{\partial}{\partial X} \left(\frac{\partial x}{\partial t} - K \left(\frac{\partial x}{\partial X} \right)^{-1} \frac{\partial p}{\partial X} \right) = 0, \quad (2)$$

where X, x are Lagrangian and Eulerian coordinates with $0 < X < L$, t is time, S is the first Piola–Kirchhoff stress without contributions from swelling or hydrodynamic pressure, $\theta_{s,0}$ is the scaffold volume fraction of the undeformed sample (sometimes known as the solid volume fraction), Q_s is the fixed charge per unit area on the scaffold surface within the pores, ϵ_f is the permittivity of interstitial fluid, p is the sum of the hydrodynamic and swelling pressures, $K\eta$ is the permeability of the deformed body, and η is the interstitial fluid viscosity. A constitutive relationship is needed to specify S ; we follow other authors (DiSilvestro and Suh, 2001; DiSilvestro et al., 2001; Whiteley and Gaffney, 2020)

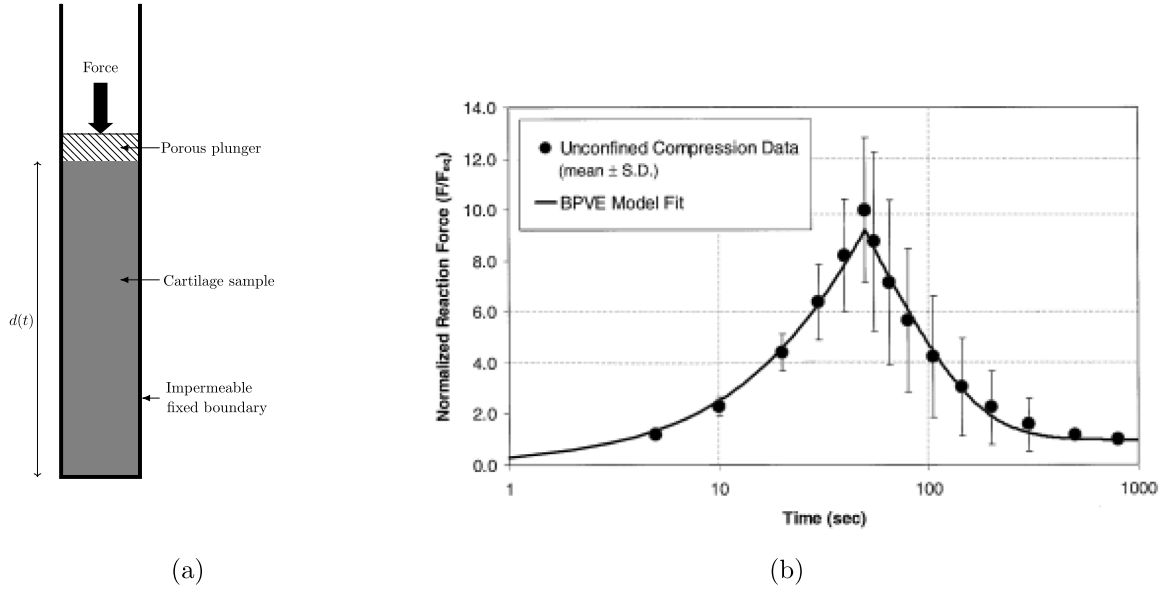


Fig. 3. (a) A schematic representation of the confined compression experiment. (b) An exemplar plot of the force exerted on the porous plunger by the cartilage during the combined compression experiment – reprinted from DiSilvestro and Suh (2001): Journal of Biomechanics, vol. 34, M. DiSilvestro and J-K.H. Suh, A cross-validation of the biphasic poroviscoelastic model of articular cartilage in unconfined compression, indentation and confined compression, 519–525, Copyright (2001), with permission from Elsevier.

and set

$$S = \frac{3\lambda + 5\mu}{3} \left(\frac{\partial x}{\partial X} - 1 \right) + \sum_{n=1}^{N_{\text{relax}}} Q_n^{\text{visc}}, \quad (3)$$

$$\frac{\partial Q_n^{\text{visc}}}{\partial t} + \frac{1}{\tau_n} Q_n^{\text{visc}} = G_v \mu \frac{\partial^2 x}{\partial t \partial X}, \quad n = 1, 2, \dots, N_{\text{relax}}, \quad (4)$$

where λ, μ are Lamé coefficients, G_v is a dimensionless scalar, and there are N_{relax} viscoelastic relaxation processes with time constants τ_n contributing Q_n^{visc} to S for $n = 1, 2, \dots, N_{\text{relax}}$.

The flux of fluid per unit area relative to the tissue, F , is given by

$$F = -K \left(\frac{\partial x}{\partial X} \right)^{-1} \frac{\partial p}{\partial X}. \quad (5)$$

The boundary at $X = 0$ denotes the tidemark (Fig. 2B), where the deep cartilage zone sharply transitions to the calcified zone, with the latter reported to be substantially stiffer and indicated to be far less permeable compared to the other cartilage layers, as detailed in the Appendix. Hence suitable boundary conditions are those associated with a fixed and impermeable interface at $X = 0$, and thus

$$x = 0, \quad \frac{\partial p}{\partial X} = 0. \quad (6)$$

The compression experiment specifies the location of the top of the sample. We assume that the fluid at the top of the sample is at atmospheric pressure. Boundary conditions at $X = L$ are then

$$x = d(t), \quad p = P_0, \quad (7)$$

where $d(t)$ is given by the location of the plunger that controls compression as illustrated in Fig. 3(a), and P_0 is atmospheric pressure. Initial conditions $x = x_0(X)$ are determined by the initial deformation being due only to swelling, and we also set $Q_n^{\text{visc}} = 0$ initially for $n = 1, 2, \dots, N_{\text{relax}}$.

2.1. Estimation of $x_0(X)$ and L

As the sample is initially deformed due to swelling we do not know the undeformed length L , the Lagrangian coordinates X , or the undeformed scaffold volume fraction $\theta_{s,0}(X)$ that are required to solve Eqs. (1)–(7). We may, however, infer these quantities from the deformed length due to swelling L_{swell} and scaffold volume fraction due to swelling $\theta_{s,\text{swell}}$. We first note that, as the scaffold volume fraction in

the deformed body θ_s satisfies $\theta_s = \theta_{s,0}/J$ where $J = \partial x/\partial X$ is the Jacobian of the deformation gradient tensor (Whiteley and Gaffney, 2020), we have

$$\theta_{s,\text{swell}} = \theta_{s,0} \left(\frac{\partial x_0}{\partial X} \right)^{-1}.$$

The initial deformation $x_0(X)$, due only to swelling rather than compression, then satisfies Eqs. (1)–(7) with the exception that the first boundary condition in Eq. (7) is changed so that the total stress is equal to atmospheric pressure at $X = L$:

$$S - \theta_{s,0} \left(\frac{\partial x_0}{\partial X} \right)^{-1} \frac{Q_s^2}{\epsilon_f} - p = -P_0.$$

These equations have a solution that satisfies

$$\frac{\partial x_0}{\partial X} = 1 + \frac{3\theta_{s,\text{swell}} Q_s^2}{\epsilon_f (3\lambda + 5\mu)}, \quad p = P_0. \quad (8)$$

The equation for x_0 may be integrated using the first boundary condition from Eq. (6) as an initial condition. This allows us to determine the Lagrangian coordinates X and the undeformed length L of the sample.

Eq. (8) allows us to write Eqs. (1)–(7) using the known coordinates of the sample due to swelling, x_0 , rather than the unknown Lagrangian coordinates X . For $0 < x_0 < L_{\text{swell}}$, noting that $x_0 = x_0(X)$:

$$\frac{\partial}{\partial x_0} \left(S - \theta_{s,\text{swell}} \left(\frac{\partial x}{\partial x_0} \right)^{-1} \frac{Q_s^2}{\epsilon_f} - p \right) = 0, \quad (9)$$

$$\frac{\partial}{\partial x_0} \left(\frac{\partial x}{\partial t} - K \left(\frac{\partial x}{\partial x_0} \right)^{-1} \frac{\partial p}{\partial x_0} \right) = 0, \quad (10)$$

$$S = \frac{3\lambda + 5\mu}{3} \left(\frac{\partial x}{\partial x_0} \frac{\partial x_0}{\partial X} - 1 \right) + \sum_{n=1}^{N_{\text{relax}}} Q_n^{\text{visc}}, \quad (11)$$

$$\frac{\partial Q_n^{\text{visc}}}{\partial t} + \frac{1}{\tau_n} Q_n^{\text{visc}} = G_v \mu \frac{\partial^2 x}{\partial t \partial x_0} \frac{\partial x_0}{\partial X}, \quad n = 1, 2, \dots, N_{\text{relax}}. \quad (12)$$

3. Modelling assumptions and parameterisation of the model

We now specify the spatial variations in material properties that were discussed in Section 1, and justify our choices of constitutive relationships for these parameters. We write down the material properties for normal cartilage in Section 3.1, explain how they may be modified for osteoarthritic pathophysiology in Section 3.2, and present illustrative solutions to the governing equations in Section 3.3. We conclude our discussion of parameterisation of the model by giving an example of a parameter set in Section 3.4 where the governing equations written down in Section 2 do not have a solution, and explain why this is the case.

3.1. Normal, physiological tissue

The cartilage scaffold volume fraction is indicated to be higher in the calcified layer and deep layer compared to the superficial layer (Klika et al., 2019; Wilson et al., 2006, 2007). In the absence of experimental evidence that specifies variations in cartilage scaffold volume as a function of depth into cartilage tissue we assume that there is a linear relationship between scaffold volume fraction and depth (or equivalently that the depth dependence is sufficiently small to allow a linear approximation). The assumption of linear dependence with depth into the cartilage will also be used when specifying other quantities with depth dependence for the same reason. Assuming further that these values are measured in cartilage that is deformed only due to swelling, we write

$$\theta_{s,swell}(x_0) = \frac{(L_{swell} - x_0)\theta_0 + x_0\theta_1}{L_{swell}}. \quad (13)$$

Here θ_0 is the scaffold volume fraction at the tidemark (Fig. 2B, where $x_0 = 0$) and θ_1 is the scaffold volume in the superficial layer of the cartilage (where $x_0 = L_{swell}$).

Based on many observations, for example from bovine (Schinagl et al., 1997) and human (Antons et al., 2018) cartilage as summarised in Fig. 2, cartilage stiffness decreases as we move away from the deep region into the superficial layer. Hence we approximate the Young's modulus E by a linear function of depth in the swollen sample:

$$E(x_0) = \frac{(L_{swell} - x_0)E_0 + x_0E_1}{L_{swell}},$$

where E_0 is the Young's modulus at the tidemark, and E_1 is the Young's modulus in the superficial zone. With ν denoting the Poisson ratio, the Lamé coefficients λ, μ are given by

$$\mu(x_0) = \frac{E(x_0)}{2(1 + \nu)}, \quad \lambda(x_0) = \frac{E(x_0)\nu}{(1 + \nu)(1 - 2\nu)}. \quad (14)$$

Furthermore, the baseline value of the Poisson ratio in Table 1 is given by $\nu = 0.1 \ll 1$ and only features in the model via the following linear combinations of Lamé coefficients:

$$\mu = \frac{E}{2(1 + \nu)} = \frac{E}{2} (1 - \nu + O(\nu^2)) \approx \frac{E}{2},$$

$$3\lambda + 5\mu = \frac{E}{1 + \nu} \left(\frac{3\nu}{1 - 2\nu} + \frac{5}{2} \right) = \frac{5E}{2} \left(1 + \frac{\nu}{5} + O(\nu^2) \right) \approx \frac{5}{2} E.$$

Thus at leading order the Poisson ratio, and hence its variation if it were to be included in a sensitivity analysis, drops out and thus would not have a significant impact on the model. Hence the Poisson ratio is treated as a constant at its base value; this rational simplification is also motivated by the fact that each degree of freedom varied in the global sensitivity analysis below adds significantly to the computational cost of the analysis.

In previous work (Whiteley and Gaffney, 2020) we have used the Kozeny-Carman formula to relate porosity to permeability, a relation developed to model permeability in rocks (Han et al., 2019). A relationship that has previously been used to model cartilage permeability (Wilson et al., 2006), and is consistent with the observations of Maroudas

(1968) and Maroudas and Bullough (1968), may be written in the form

$$K = \bar{K} \left(\frac{\theta_{s,0}}{1 - \theta_f} \right)^{1.339}, \quad (15)$$

where \bar{K} depends only on the spatial coordinate, and $\theta_f = 1 - \theta_s$ is the porosity of the deformed body. Should high levels of compression be encountered Eq. (15) may become unphysiological as Eq. (5) predicts a non-zero fluid flux relative to the cartilage tissue even when $\theta_f = 0$, i.e. where no fluid exists. This violates the principle of conservation of mass that underpins the derivation of Eq. (2). We therefore modify Eq. (15) by introducing a scaling factor of $\theta_f/\theta_{f,0}$, where $\theta_{f,0}$ is the porosity of the undeformed body; this will have no effect on the permeability of the undeformed sample, but will give zero permeability – and consequently zero fluid flux – when $\theta_f = 0$. We then obtain

$$K = \bar{K} \frac{\theta_f}{1 - \theta_{s,0}} \left(\frac{\theta_{s,0}}{1 - \theta_f} \right)^{1.339}. \quad (16)$$

The permeability of cartilage increases as we move from the tidemark into the superficial zone (Maroudas, 1968; Maroudas and Bullough, 1968). We model this by setting

$$\bar{K}(x_0) = \frac{(L_{swell} - x_0)\bar{K}_0 + x_0\bar{K}_1}{L_{swell}}, \quad (17)$$

where \bar{K}_0 is the value of \bar{K} at the tidemark, and \bar{K}_1 is the value of \bar{K} in the superficial zone.

The derivation of the term that models swelling in Eq. (1) is underpinned by the use of the fixed charge density on the pore surface at the microscale, Q_s , Whiteley and Gaffney (2020). It has been reported that the charge density per unit volume is lower in the superficial zone than in the deep zone (e.g. Maroudas and Bullough (1968)), as also observed in Fig. 1. The term that contains Q_s in Eq. (9) is multiplied by $\theta_{s,swell}$. By noting that $\theta_{s,swell}$ decreases from the tidemark to the superficial layer – as encapsulated by Eq. (13) – we see that a decrease in charge per unit volume is captured by setting Q_s to be constant. The value of Q_s is chosen to fit with the deformation due only to swelling, which is estimated to cause a strain in the range of 0.03–0.1 (Lai et al., 1991). To estimate a value for Q_s we calculate L_{swell}/L as a function of Q_s by solving Eq. (8) as described in Section 2.1, setting other parameters to the base values given in Table 1, and plot the results in Fig. 4. The estimates of strain for deformation due only to swelling given by Lai et al. (1991) suggest that Q_s should be in the range between approximately -0.01 and -0.005 A s m⁻².

3.2. Osteoarthritic tissue

As reported in the Introduction, osteoarthritic tissue can feature higher permeability and lower charge density magnitude in the superficial layer of cartilage (Saarakkala et al., 2010; Setton et al., 1993). The higher permeability in the superficial layer is modelled by adding an extra term to Eq. (17) to give

$$\bar{K}(x_0) = \frac{(L_{swell} - x_0)\bar{K}_0 + x_0\bar{K}_1}{L_{swell}} + \frac{\bar{K}_{OA}}{1 + \exp(-\gamma_{K,OA}(x_0 - \hat{x}_{K,OA}))}, \quad (18)$$

for constants \bar{K}_{OA} , $\gamma_{K,OA}$, $\hat{x}_{K,OA}$. The lower charge density in the superficial layer is modelled by scaling the charge per unit area so that

$$Q_s(x_0) = \frac{Q_s}{1 + \exp(\gamma_{Q,OA}(x_0 - \hat{x}_{Q,OA}))}, \quad (19)$$

for constants $\gamma_{Q,OA}$, $\hat{x}_{Q,OA}$. We choose parameters that give the qualitative behaviour expected for early stages of osteoarthritic tissue discussed in the Introduction. These parameters are given in Table 1, and the resulting $\bar{K}(x_0)$ and $Q_s(x_0)$ calculated using these parameters are plotted in Fig. 5.

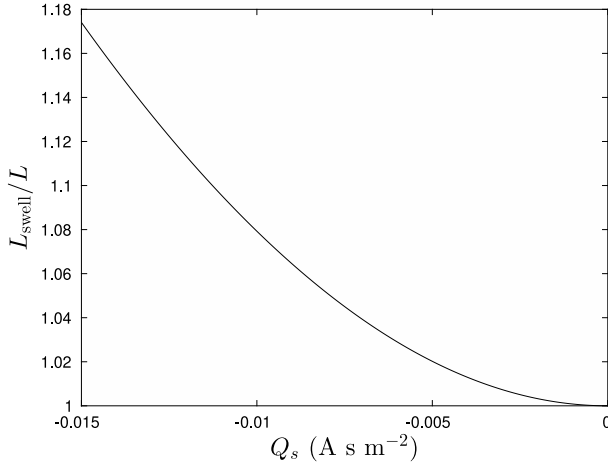


Fig. 4. The ratio L_{swell}/L as a function of scaffold surface fixed charge density Q_s , when deformation of a one dimensional sample fixed at one end is due only to swelling. L_{swell} represents the length of the sample after swelling, and L the length in the absence of swelling.

Table 1

Parameter values used in this study. The subscript 0 represents a quantity at the tidemark and a subscript 1 represents a quantity in the superficial layer. Note that the Young's modulus E_0 is from Schinagl et al. (1997) for measurements from a 125 μm deep section of cartilage that excludes the deepest 250 μm of the sample where the calcified layer is found, and thus is taken to represent the Young's modulus of the deep zone near the tidemark.

Parameter	Base value	Reference
L_{swell}	$1.28 \times 10^{-3} \text{ m}$	Whiteley and Gaffney (2020)
E_0	$1.14 \times 10^6 \text{ N m}^{-2}$	Schinagl et al. (1997)
E_1	$7.9 \times 10^4 \text{ N m}^{-2}$	Schinagl et al. (1997)
ν	0.1	DiSilvestro and Suh (2001)
θ_0	0.3	Klika et al. (2019)
θ_1	0.15	Klika et al. (2019)
Q_s	-0.01 A s m^{-2}	See discussion in text
\bar{K}_0	$1.72 \times 10^{-15} \text{ m}^4 \text{ N}^{-1} \text{ s}^{-1}$	Whiteley and Gaffney (2020)
\bar{K}_1	$2\bar{K}_0$	Maroudas (1968)
ϵ_f	$6.93 \times 10^{-10} \text{ A}^2 \text{ s}^2 \text{ N}^{-1} \text{ m}^{-2}$	Whiteley and Gaffney (2020)
N_{relax}	3	DiSilvestro and Suh (2001)
τ_n	0.62 s, 7.26 s, 85 s	DiSilvestro and Suh (2001)
G_v	5.32	DiSilvestro and Suh (2001)
$\gamma_{Q,OA}$	$20/L_{\text{swell}}$	See discussion in text
$\hat{x}_{Q,OA}$	$0.8L_{\text{swell}}$	See discussion in text
\bar{K}_{OA}	$4\bar{K}_0$ or $40\bar{K}_0$	See discussion in text
$\gamma_{K,OA}$	$100/L_{\text{swell}}$	See discussion in text
$\hat{x}_{K,OA}$	$0.95L_{\text{swell}}$	See discussion in text

3.3. Exemplar simulations

In Fig. 6 we plot the numerical solution of the governing equations using the parameters for normal tissue given in Table 1. We plot the deformed coordinate x in Fig. 6(a), the pressure relative to the ambient pressure in Fig. 6(b), the porosity in Fig. 6(c), and K in Fig. 6(d). Note that the horizontal axes in these figures is different; we have chosen axis limits to demonstrate the relevant features with clarity. In each of these figures we plot the solution as a function of x_0 at the midpoint of the compressive phase ($t = 25 \text{ s}$), the end of the compressive phase ($t = 50 \text{ s}$), and two times in the relaxation phase ($t = 75, 100 \text{ s}$). We see in Fig. 6(b) that the pressure rises during the compressive phase, and then falls during the relaxation phase. Even at $t = 100 \text{ s}$ there is a negative pressure gradient, causing a flux of fluid out of the sample, explaining the change in deformation seen in Fig. 6(a) after the end of the compressive phase. We see in Fig. 6(c) that the porosity decreases significantly in tissue close to the plunger, in the cartilage superficial region, during the compressive phase, and then increases during the relaxation phase. This observation on the porosity

is a significant contribution to the permeability behaviour, plotted in Fig. 6(d). Moving deeper into the cartilage tissue, further away from the plunger, the porosity does not vary significantly, and the increase in K – that is the permeability per unit interstitial fluid viscosity – is due to the increase in \bar{K} as prescribed by Eq. (17). Close to the plunger, in the cartilage superficial region where the porosity does vary significantly, Eq. (16) explains the decrease in K .

In Fig. 7 we repeat the simulations presented in Fig. 6, but using parameters representative of osteoarthritic tissue with $\bar{K}_{OA} = 4\bar{K}_0$. One key difference between the simulations of normal tissue and osteoarthritic tissue is the existence of a local maximum in the pressure during the compressive phase seen in osteoarthritic tissue in Fig. 7(b). Using Eq. (5) this implies that, for values of x_0 to the left of the peak, fluid is squeezed away from the plunger. We note that the absolute values of $p - P_0$ are considerably smaller than for normal tissue, and so this flux is actually very small. We also note that the prediction for K in normal tissue has a sharp gradient in the opposite direction of K for osteoarthritic cartilage in the superficial region, and the latter also exhibits a local minimum close to the plunger. This is caused by K initially decreasing due to the decrease in porosity (as was the case for normal tissue), but then increasing due to the increasing \bar{K} in the superficial zone seen in Fig. 5(a).

3.4. A warning example

We now demonstrate that the governing equations do not have a solution for some choices of parameters. We repeat the simulation described in Section 3.3, but with the exception that the compression time is reduced to 20 s. In Fig. 8 we plot: (a) the deformed coordinate x ; (b) the pressure p relative to P_0 ; (c) the porosity, θ_f ; and (d) the permeability per unit interstitial fluid viscosity, K , as a function of x_0 for various times t . Note that the horizontal axis used in these plots differs; some plots are clearer when only plotting values of x_0 in the cartilage superficial region, close to the plunger that is used to control compression. We see in Fig. 8(a) that, as time increases, significant compression beyond the initial compression of the sample to $0.9L_{\text{swell}}$ occurs only close to the plunger. In Fig. 8(b) we see that spatial variations in pressure – and therefore spatial variations in fluid flux – also occur only close to the plunger as time increases. As a consequence of these observations on deformation we see in Fig. 8(c) that the porosity decreases substantially in the region of the plunger, and that the porosity becomes zero adjacent to the plunger, where $x_0 = 1.28 \times 10^{-3} \text{ m}$, at time $t = 7.74 \text{ s}$ during the compression phase. This has the effect that the permeability also becomes zero adjacent to the plunger, as seen in Fig. 8(d) where $K = 0$. When $K = 0$ Eq. (5) predicts that it is not possible for any more fluid to be expelled from the sample through the plunger. As the derivation of the governing equations assumes that both the fluid and the solid scaffold are incompressible (Whiteley and Gaffney, 2020) the assumptions included in the model do not allow the plunger to compress the tissue any further, and the one-dimensional model described in Section 2 is no longer suitable. In practice, it might be anticipated that the scaffold would start compressing, with a volume shrinkage of the solid phase, or deformations in higher spatial dimensions manifest, though the prospects of such additional complexities are not considered in the present model.

The only difference between the two simulations presented in Figs. 6 and 8 is the compression time – all other parameters are identical. Whether or not we can reach a steady state solution for a given parameter set in this one dimensional model may depend on the compression time simulated, with slower compression times more likely to allow the sample to reach a steady state solution without encountering a situation where $\theta_f \leq 0$. As a consequence there will be limited parameter sets where an unsteady simulation fails, yet exactly the same parameter set does allow a steady state solution. We include this example to illustrate why some parameter sets will be rejected in the sensitivity analysis.

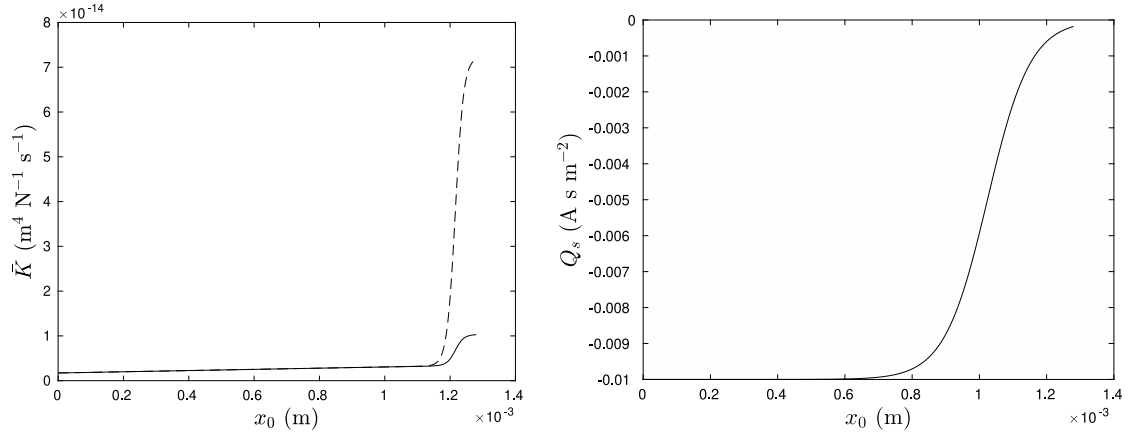


Fig. 5. \bar{K} and scaffold surface charge density as a function of x_0 for osteoarthritic tissue. We show \bar{K} for both the case where $\bar{K}_{OA} = 4\bar{K}_0$ (solid line) and the case where $\bar{K}_{OA} = 40\bar{K}_0$ (broken line).

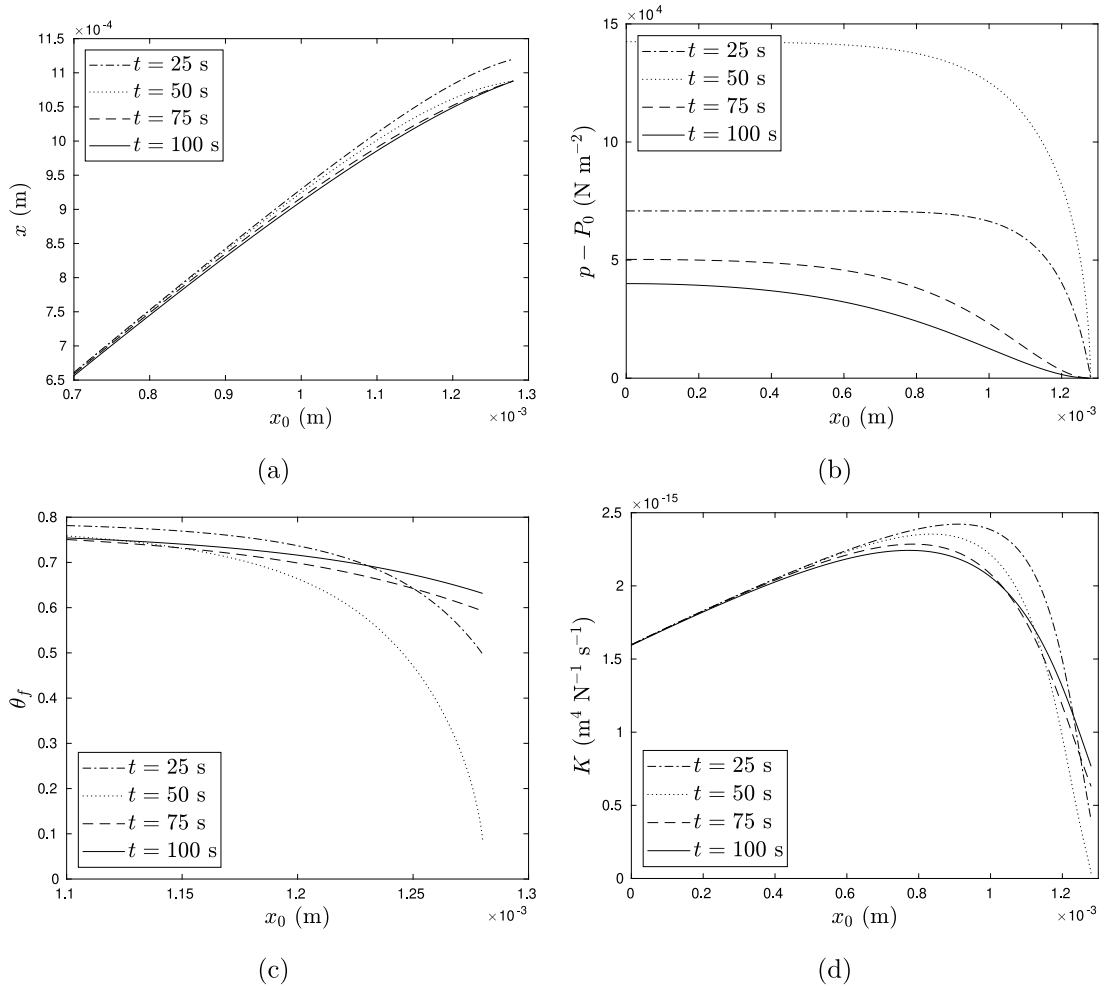


Fig. 6. Results of the simulation described in Section 3.3 using parameters representative of normal tissue, plotted as a function of x_0 at various times: (a) the deformed coordinate; (b) the pressure relative to the ambient pressure; (c) the porosity; and (d) the permeability per unit interstitial fluid viscosity, K . Note that the horizontal axis varies between plots.

4. Sensitivity analysis

Sensitivity analyses may be conducted using many techniques, such as Sobol, Fourier Analysis Sensitivity Testing (FAST), extended Fourier Analysis Sensitivity Testing (eFAST) (Marino et al., 2008; Renardy

et al., 2021; Saltelli et al., 1999) or Principal Component Analysis (PCA) (Jolliffe and Cadima, 2016). The Sobol, FAST and eFAST approaches require that a solution to the governing equations exists for all parameter sets sampled, but we observed in Section 3.4 that this is not the case for our model. Nevertheless, either of the FAST or eFAST

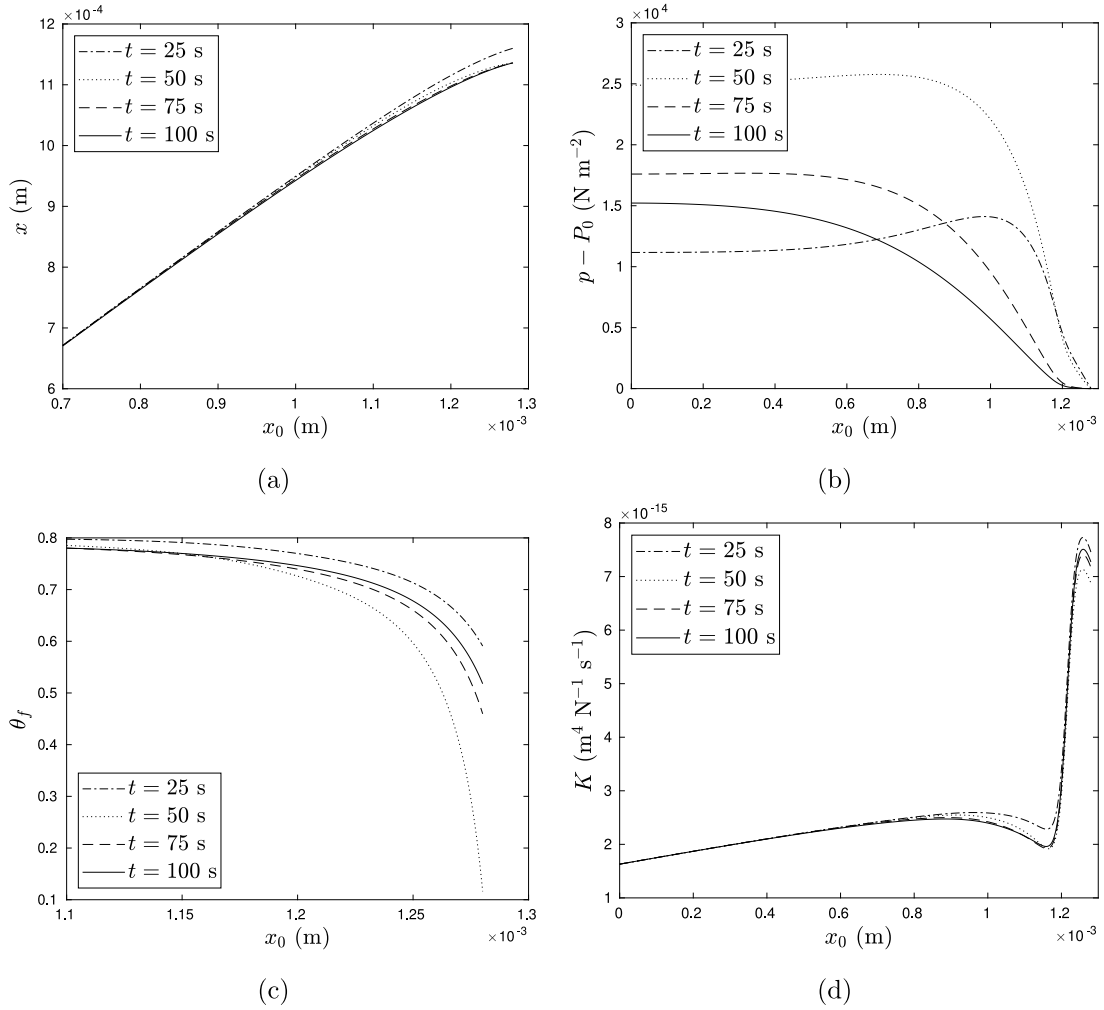


Fig. 7. Results of the simulation described in Section 3.3 using parameters representative of osteoarthritic tissue (with $\bar{K}_{OA} = 4\bar{K}_0$) plotted as a function of x_0 at various times: (a) the deformed coordinate; (b) the pressure relative to the ambient pressure; (c) the porosity; and (d) the permeability per unit interstitial fluid viscosity, K . Note that the horizontal axis varies between plots.

methods in particular provide us with an algorithm to efficiently sample points within the parameter space that may be analysed using PCA, which we now describe.

Let a model include N parameters $\alpha_1, \dots, \alpha_N$ that may be varied, and let $y = F(\alpha_1, \dots, \alpha_N)$ be an output from the model. A different frequency ω_i is allocated to each parameter α_i ; suitable values of the frequencies may be found in [Schaibly and Shuler \(1973\)](#). We then set

$$N_s = 2M \max_i \omega_i + 1,$$

where M is an integer with $M \geq 4$, and sample at the points s_k defined by

$$s_k = \frac{\pi(2k - N_s - 1)}{N_s}, \quad k = 1, 2, 3, \dots, N_s.$$

At each sampled value of s_k the parameters used in the model are given by

$$\alpha_i = \alpha_{i,0} + (\alpha_{i,1} - \alpha_{i,0}) \left(\frac{1}{2} + \frac{1}{\pi} \arcsin(\sin(\omega_i s_k + \phi_i)) \right), \quad i = 1, 2, \dots, N,$$

where ϕ_i , $i = 1, 2, \dots, N$ are uniformly sampled in the interval $0 \leq \phi_i < 2\pi$, and $\alpha_{i,0}, \alpha_{i,1}$ are the minimum and maximum values of α_i that are to be considered. This process may be repeated N_R times, with the ϕ_i re-sampled on each repeat. Each sampled value of s_k allows us to simulate an output y_k .

To perform a PCA analysis a $N_s N_R \times (N+1)$ matrix A is constructed, where row i of A contains the sampled parameter set $\alpha_1, \dots, \alpha_N$ arising

from s_i in columns 1 to N , and the output from the model for this parameter set in column $N+1$. The matrix B is then derived from A by first subtracting the mean of column j from all values in column j , and then scaling column j so that the entries of column j have zero mean and unit variance. The covariance matrix $S = B^T B$ then has $N+1$ positive eigenvalues $\lambda_1 \geq \lambda_2 \geq \dots \geq \lambda_{N+1}$. Let \mathbf{e} be an eigenvector associated with the largest eigenvalue λ_1 , which we take to be distinct noting that generalisation to a repeated largest eigenvalue has not been necessary in this study. A sensitivity index for parameter n is then given by $|e_n/e_{N+1}|$ for $n = 1, 2, \dots, N$, where e_n is the n 'th component of \mathbf{e} .

The total stress in the cartilage sample, S_{tot} is given by

$$S_{\text{tot}} = S - \theta_{s,0} \left(\frac{\partial x}{\partial X} \right)^{-1} \frac{Q_s^2}{\epsilon_f} - p.$$

Using Eq. (9) we see that S_{tot} is independent of x_0 , and so $S_{\text{tot}} = S_{\text{tot}}(t)$. The outputs we consider are: (i) S_{tot} ; (ii) the maximum strain within the sample at a given time t ; and (iii) the minimum porosity within the sample at a given time t . The first of these outputs is chosen as this is the quantity usually measured when a compression test experiment is performed. The second quantity is an indicator of the potential for damage to cartilage tissue. The final quantity indicates when the model is likely to fail, as discussed in Section 3.4. As all of these outputs are functions only of t , for each value of t we may perform a PCA analysis using each of the outputs separately.

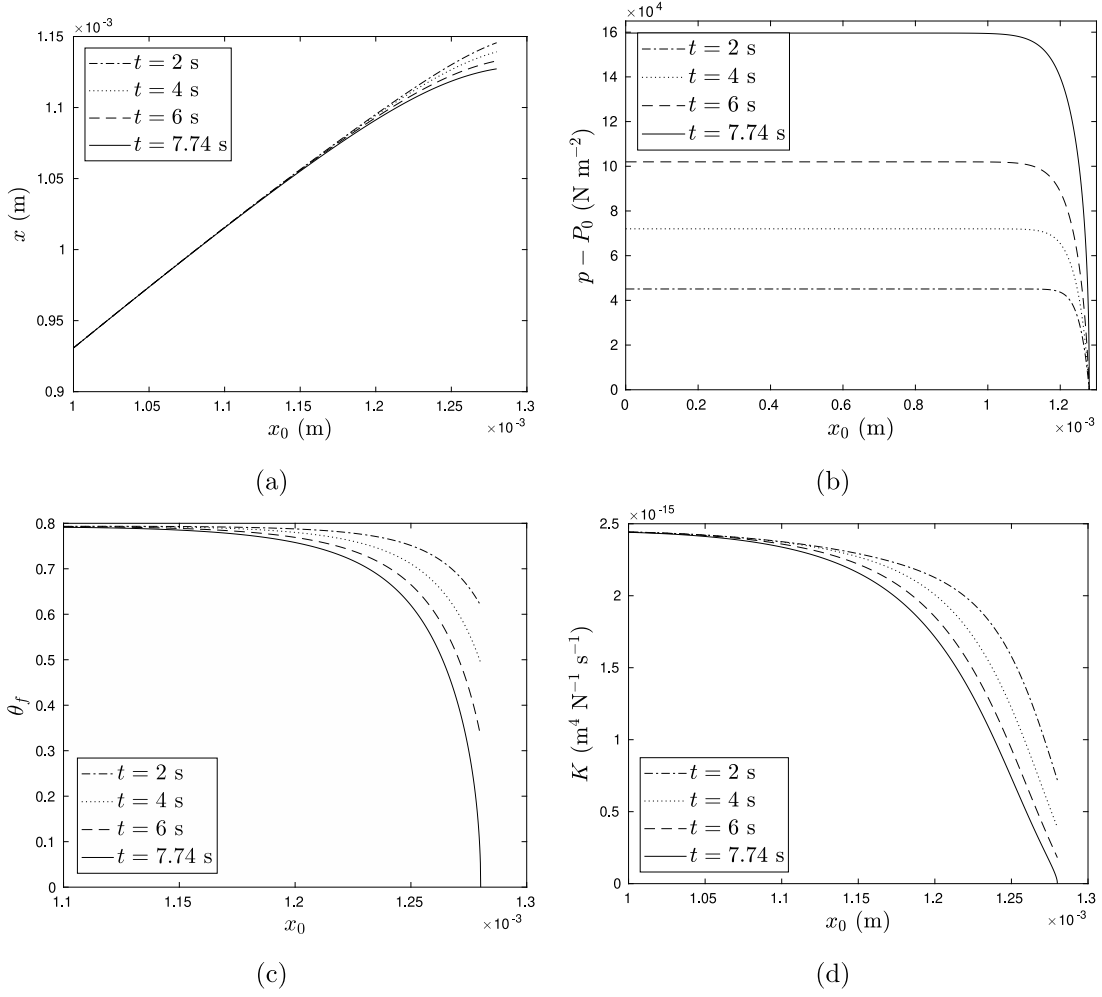


Fig. 8. Results of the simulation described in Section 3.4, plotted as a function of x_0 at various times: (a) the deformed coordinate; (b) the pressure relative to the ambient pressure; (c) the porosity; and (d) the permeability per unit interstitial fluid viscosity, K . Note that the horizontal axis varies between plots.

4.1. PCA analysis of static loading

For steady state simulations of normal cartilage tissue we compute a steady state compression to 0.85 of the swollen length L_{swell} , i.e. the compression of the sample at the end of the compression test experiment. In the steady state we have $\partial x / \partial t = 0$. Using the pressure boundary conditions in Eqs. (6) and (7) we may integrate Eq. (2) to deduce that $p = P_0$ throughout the cartilage in steady state, and that the solution is independent of K . Similarly, we may use Eq. (4) to deduce that $Q_n^{\text{visc}} = 0$ in a steady state solution. As a consequence of these two observations the steady state solution is independent of the parameters \bar{K}_0 , \bar{K}_1 and G_v , and in our PCA analysis of the steady state solution we vary the parameters E_0 , γ , θ_0 , Q_s , α for normal cartilage tissue, where $\gamma = E_1/E_0$ and $\alpha = \theta_1/\theta_0$; varying γ and α rather than E_1 and θ_1 allows us to investigate the effect of heterogeneity in E and $\theta_{s,\text{swell}}$ and ensures that the scaffold volume fraction is always lower in the superficial region compared to the tidemark for all parameter sets.

The base values of the model parameters are given in Table 1, which also yield the base value of $\gamma = E_1/E_0$ and $\alpha = \theta_1/\theta_0$. Each parameter of the set $\{E_0, \gamma, \theta_0, Q_s, \alpha\}$ is sampled as described in Section 4 in a multiplicative range from 0.6 of the base value to 1.4 of the base value; this variation was sufficiently small to ensure that porosity predicted by the steady state solution was positive for all parameter sets sampled.

We repeat the PCA analysis for simulated osteoarthritic tissue in a similar manner. We will see later, when conducting a PCA analysis for osteoarthritic tissue, that an extremely high proportion of simulations

will be rejected if we subject tissue in these simulations to the same compression as for normal tissue, though this difficulty was not nearly as extensive for normal cartilage tissue. To allow our statistical analysis of the simulation of osteoarthritic tissue to include a sufficiently large number of samples that are not rejected, we reduce the magnitude of the simulated compression of osteoarthritic tissue, and thus use a more modest compression to 0.8875 of the swollen length in the osteoarthritic cartilage simulations, i.e. three-quarters of the compression used for the normal cartilage tissue simulations discussed above, to prevent this difficulty. We also vary the parameter $\hat{x}_{Q,OA}$, which controls the region where the magnitude of fixed charge begins to fall, as can be seen in Eq. (19) and Fig. 5(b).

The results of the PCA analyses are given in Table 2 for both normal and osteoarthritic simulations. We see that E_0 and Q_s are predicted to be the most sensitive parameters for normal tissue when S_{tot} is used as the output from the model, and that Q_s is the most important parameter when the output from the model is the maximum strain. When the minimum porosity is used as the output from the model θ_0 is the comfortably the most dominant parameter. In contrast, for osteoarthritic tissue it is the parameters E_0 and γ that are the most influential when S_{tot} is used as the output from the model. When the maximum strain is used as the output, the parameter γ is by some distance the dominant parameter. The parameters α , θ_0 and γ are the most significant parameters when the output from the model is the minimum porosity. The parameter $\hat{x}_{Q,OA}$ was not significant for any output of the model for osteoarthritic tissue.

Table 2

The sensitivities for the steady state simulations.

Parameter	Normal			Osteoarthritic		
	S_{tot}	max strain	min θ_f	S_{tot}	max strain	min θ_f
E_0	0.8538	0.3150	0.1032	0.9354	0.1185	0.0054
γ	0.1864	0.1611	0.1411	0.2774	0.9397	0.5375
θ_0	0.2145	0.3441	0.9247	0.1178	0.2194	0.6884
α	0.1457	0.3692	0.2595	0.0700	0.2616	0.4137
Q_s	0.4110	0.7873	0.2167	0.1799	0.2207	0.0590
$\hat{x}_{Q,OA}$				0.0135	0.0326	0.0183

4.2. PCA analysis of dynamic loading

We simulate data from the confined compression experiment described in the Introduction for normal cartilage tissue; the swollen sample is compressed to 0.9 of its swollen length and, after the force on the plunger has reached a steady state, the sample is compressed to 0.85 of its swollen length over 50 s and then held at this compressed length for a further 450 s. For normal tissue we vary the parameters $E_0, \gamma, \theta_0, \alpha, Q_s, \bar{K}_0, \beta = \bar{K}_1/\bar{K}_0, G_v$ between 0.6 and 1.4 of their base values given in Table 1, rejecting the output from any parameter set where the porosity becomes negative at any point as discussed in Section 3.4. For osteoarthritic tissue we also vary the parameter $\hat{x}_{Q,OA}$. As with the steady state PCA analysis for osteoarthritic cartilage tissue in Section 4.1 we use only three-quarters of the compression of normal tissue when modelling osteoarthritic tissue to ensure that the porosity is positive for a significant proportion of parameter sets sampled, i.e. for osteoarthritic tissue we start from a compression to 0.925 of the swollen length, and compress to 0.8875 of the swollen length.

The PCA sensitivity indices for each parameter for normal tissue are plotted in Fig. 9 as a function of t , where solid lines represent indices calculated using S_{tot} as the model output, broken lines represent indices calculated using the maximum strain as the model output, and dotted lines represent indices calculated using the minimum porosity as the model output. A proportion of 0.288 of the parameter sets were rejected as a value of $\theta_f = 0$ occurred during the compression phase. We explained in Section 4.1 that steady state solutions are independent of the parameters \bar{K}_0, β and G_v ; the sensitivity indices of these parameters approach zero as time increases and a steady state is approached for all outputs, as expected. These parameters do, however, have sensitivity indices of a significant size at earlier times in the simulation. Other parameters have differing levels of influence at different times in the simulation, with all parameters playing a significant role at some point in the simulations. We might expect that the values of the sensitivity indices would approach the corresponding values given in Table 2 for steady state simulations. Although the values are similar they are not equal. This is due to the rejection of some parameter sets for the unsteady simulations as discussed in Section 3.4 — even if a parameter set admits a steady state solution there is the possibility that a value of $\theta_f = 0$ occurs during compression before the steady state is reached if the compression is too rapid.

The PCA sensitivity indices for osteoarthritic tissue are plotted in Fig. 10 for the case of a moderate increase in superficial zone permeability, with $\bar{K}_{OA} = 4\bar{K}_0$. A proportion of 0.222 of parameter sets were rejected as a value of $\theta_f = 0$ was encountered during the compression stage of the simulation. The parameter γ is a critical parameter for all model outputs, and the parameter $\hat{x}_{Q,OA}$ is critical especially when the model output is the total force or the maximum strain. In addition E_0 was significant when S_{tot} was considered, G_v was significant in the early stages of the simulation when S_{tot} was the output considered, and the parameters θ_0, α were also dominant parameters governing the minimum porosity. Similar observations on the values of the sensitivity indices as time increases, and their relationship with the steady state sensitivity indices, apply to those discussed for a normal cartilage sample.

We now consider the case of an extensive increase in superficial zone permeability, now with $\bar{K}_{OA} = 40\bar{K}_0$, and thus further increased by an order of magnitude. A proportion of 0.171 of parameter sets were rejected due to the porosity becoming zero during the simulation using these parameters and the PCA sensitivity indices are given in Fig. 11. Comparing Figs. 10 and 11 we see that there is very little difference between the cases.

5. Discussion

We have extended a previously published poroviscoelastic model of articular cartilage (Whiteley and Gaffney, 2020) to include the spatial variation in stiffness, porosity, permeability and electric fixed charge density that are seen in both normal and osteoarthritic cartilage tissue. Even though we have used a one-dimensional version of this model in this study, the inclusion of cartilage depth dependencies in the modelling framework nonetheless necessitated a large number of parameters. Examination of illustrative simulations for the confined compression test used to investigate cartilage properties in this study, presented in Figs. 6–8, highlights that higher pressures are predicted to be supported in normal, physiological cartilage. Furthermore, these figures emphasise that pressure gradients, and thus stresses, and volume fraction change rapidly close to the superficial interface of cartilage, with relatively large deformation gradients in this region. In turn, this suggests that superficial zone surface properties in general are fundamental in the mechanical responses of cartilage, emphasising the need to consider depth variation. Examining the superficial region in further detail, recall that K is the permeability per unit interstitial fluid viscosity and thus a measure of permeability. In examining gradients of this measure for exemplar normal cartilage simulations in Fig. 6 and osteoarthritic simulations in Fig. 7, one can observe sharp gradients in the superficial region for both cases, but of opposite sign, and also that the predicted osteoarthritic profiles exhibit a local minimum, giving a first indication of predictions that the model responses will be fundamentally different in the superficial region with the onset of osteoarthritis. We also note that such observations and conclusions are based on qualitative observation and thus are generic in nature, rather than contingent on precision point parameter estimation, which may be of restricted utility given for instance the population variation highlighted in the Introduction. Analogous remarks apply more generally below, where observations are either similarly drawn from qualitative features of the modelling predictions or a global sensitivity analysis that, once more, does not require fine-scale parameter estimation.

As noted in Section 3.4, this model was also not suitable for some parameter sets as a zero porosity could be predicted. We conjecture that this could be caused either by the assumption of incompressibility, or the assumption that the cartilage deformation may be modelled using only one spatial dimension. Consequently, the non-trivial geometry of the permissible parameter space excludes many methods of global sensitivity analysis, though the use of principal components (Jolliffe and Cadima, 2016) proved practical and feasible. Hence, to pursue our primary aim of identifying the parameters that predominantly influence the major features of tissue scale mechanical response in both normal and osteoarthritic cartilage, we performed a principal component global sensitivity analysis. This analysis considered three outputs of the model: (i) the force exerted; (ii) the maximum strain; and (iii) the minimum porosity. The first of these outputs is recorded in compression tests, the second is assumed to be associated with tissue damage, and the third output indicates how close the model is to predicting zero porosity. Note that parameter sets where the model failed due to zero porosity arising were excluded from the principal component analysis.

For static loading of normal tissue, and using the force exerted as output, our analysis predicted that the Young's modulus on approaching the tidemark, E_0 , and the charge density, Q_s , were the dominant parameters. When using the maximum strain as the output Q_s was the most significant parameter. When using the minimum porosity as the

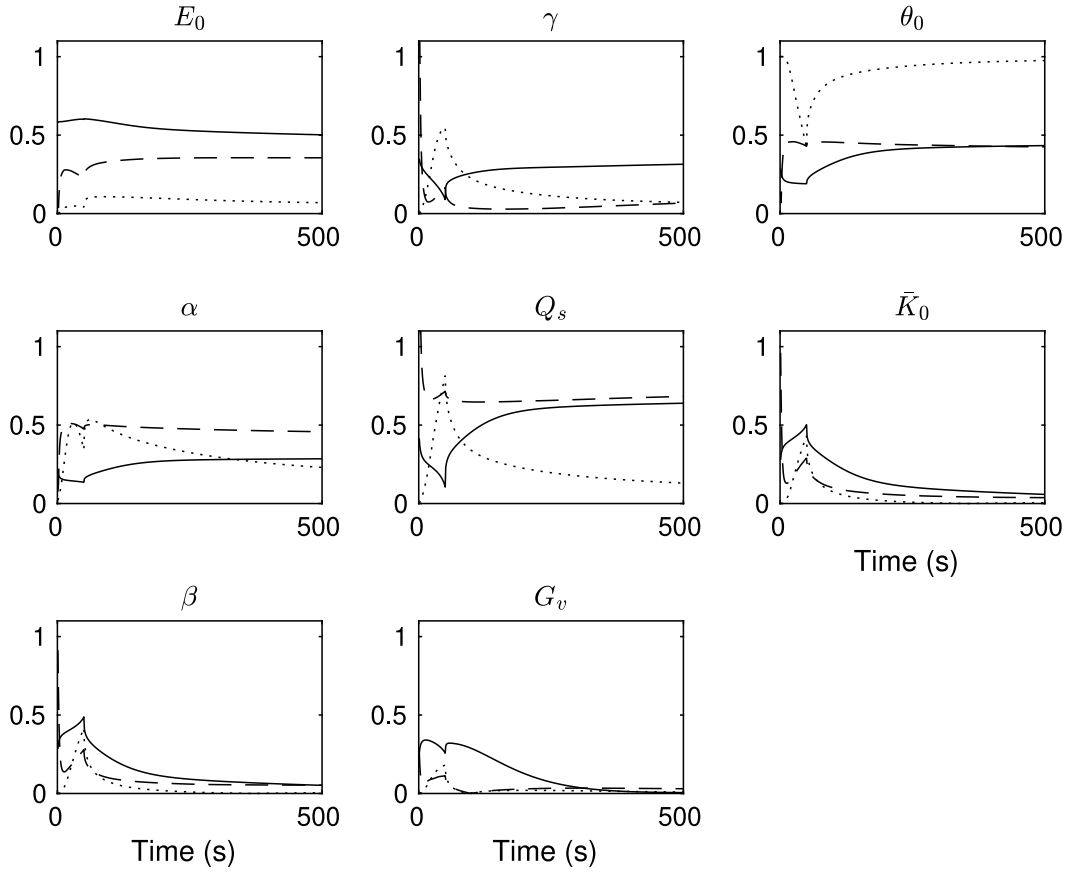


Fig. 9. PCA sensitivity indices as a function of time for simulations of normal cartilage tissue. The solid lines represent indices calculated using S_{tot} , broken lines indices calculated using the maximum strain, and dotted lines indices calculated using the minimum porosity.

output, the scaffold volume fraction on approaching the tidemark, θ_0 , was the most significant parameter. For static loading of osteoarthritic tissue γ , the ratio of the Young's modulus in the superficial layer to the Young's modulus at the tidemark between the deep and calcified layers, is a dominant parameter for all model outputs. The Young's modulus at the tidemark is the most significant parameter when model output is total force, and the porosity near the tidemark and within the superficial layers is significant when the model output is the minimum porosity. The parameter $\hat{x}_{Q,OA}$, indicating the distribution of fixed charge, was not significant for any output for static loading. An important prediction emerges — the increase in the significance of the parameter $\gamma = E_1/E_0$ for simulations of osteoarthritic tissue implies that the heterogeneity induced by the superficial zone stiffness becomes much more important in static load bearing, especially for deformation, given osteoarthritic changes associated with permeability increases and lower fixed charge.

Genuine complexity emerges in the predictions for the important parameters with dynamic loading of normal cartilage; we saw in Fig. 9 that all parameters are significant for some timepoints of the simulation for all model outputs. For dynamic loading of osteoarthritic tissue we saw in Figs. 10 and 11 that the parameter $\gamma = E_1/E_0$, the ratio of the Young's modulus in the superficial layer to the Young's modulus at the tidemark, is a key parameter for all model outputs. In contrast to static loading, the parameter $\hat{x}_{Q,OA}$ is also a key parameter in osteoarthritic simulations, especially when the model output is total force or maximum strain. The porosity at both the deep and superficial limits of cartilage are also key parameters when the model output is the minimum porosity predicted; and the parameter G_v , which controls the magnitude of the viscoelastic force, is a key parameter for early times when the output is the total force. Thus, further model simplification would not be feasible in general, as all model parameters are important

in governing mechanical response in at least one context and, as expected, cartilage response is predicted to be highly dependent on loading conditions.

Furthermore, when comparing the results of the simulations for normal tissue presented in Fig. 9 and the simulations for osteoarthritic tissue presented in Figs. 10 and 11 we note the significant increase in the sensitivity to the stiffness ratio γ with osteoarthritis, and the decrease in the sensitivity to Q_s with osteoarthritis. In common with the steady state results presented in Table 2 our results suggest that spatial variation in stiffness has a larger effect once osteoarthritis has developed in tissue, and that Q_s has less impact. We also observe that the parameter that controls the location of the region of fixed charge in osteoarthritic tissue, $\hat{x}_{Q,OA}$, is a significant parameter in dynamic simulations of osteoarthritic tissue.

More broadly, the observation from exemplar simulations in Figs. 6 and 7 that non-trivial mechanical response in both the static and dynamic scenarios is localised to the superficial zone highlights the importance of superficial cartilage properties. With this in mind, it is interesting to compare the relative dominance of the heterogeneity parameters γ, α, β between the normal and osteoarthritic simulations presented in Figs. 9–11. We see that the parameter $\gamma = E_1/E_0$ becomes more dominant for osteoarthritic tissue when the model output is the maximum strain or minimum porosity, and that the parameter $\alpha = \theta_1/\theta_0$ becomes less significant for osteoarthritic tissue when the model output is the total force or the maximum strain. The dominance of the parameter $\beta = \bar{K}_1/\bar{K}_0$ did not change extensively between simulations of normal and osteoarthritic cartilage. This interaction between parameters indicates that relatively small changes in superficial zone stiffness have a much greater effect in osteoarthritic cartilage than normal cartilage, with the opposite true for small changes in scaffold volume fraction. These may be interpreted as small degradative changes in

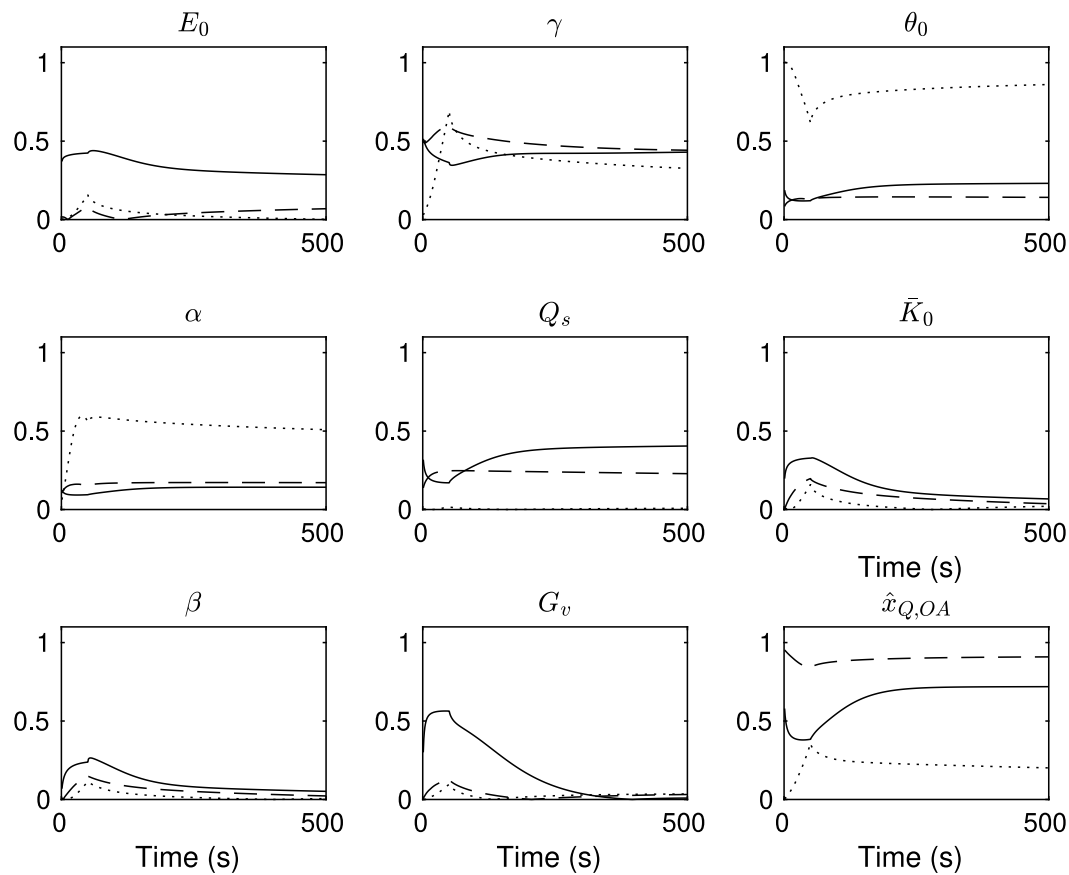


Fig. 10. PCA sensitivity indices as a function of time for simulations of osteoarthritic cartilage tissue where $\bar{K}_{OA} = 4\bar{K}_0$. The solid lines represent indices calculated using S_{tot} , broken lines indices calculated using the maximum strain, and dotted lines indices calculated using the minimum porosity.

superficial zone stiffness for normal cartilage that are not sufficient to induce significant pathology nonetheless can induce much greater, degradative-induced, changes in mechanical response when accompanied by permeability and fixed charge changes. In turn, this offers a prospective explanation for observations that mechanical parameters are not sufficient to distinguish normal cartilage from osteoarthritic cartilage (Brown et al., 2007).

More generally, this study demonstrates that global surveys of parameter space for cartilage models are feasible, despite the modelling complexity, thus suggesting many further possible studies such as the application of Bayesian parameter inference and model selection techniques. Future work may also involve elements of cartilage mechanics from the perspective of a large parameter space study, thus incorporating population-level variation within modelling studies, for instance to assess how mechanical responses might be stratified among individuals or assessing whether pre-clinical species models are predicted to be representative of the range of human pathological cartilage mechanics. Similarly, despite the computational resource challenges, there is scope to consider global parameter space studies of models with higher spatial dimensions, enabling the investigation of numerous additional features of cartilage mechanics, such as stress and strain profiles in indentation tests or sharp lateral transitions in the stiffness of subchondral bone (Radin and Rose, 1986).

In summary, we have presented a tissue level model of cartilage mechanics, with a systematic upscaling to incorporate the mechanics of fixed charge and with a depth dependence of its mechanical parameterisation to reflect our knowledge and understanding of cartilage structure. In the context of one dimensional confined compression testing, we have analysed the sensitivity across parameter space. This has highlighted that mechanical response is most sensitive to, and thus dictated by, differing parameter sets on comparing normal and

osteoarthritic cartilage and between static and dynamic loading. The model response was not uniformly insensitive to any given parameter that was varied, suggesting model simplification was not possible. Furthermore, osteoarthritis induced changes relating to permeability and fixed charge are also predicted to sensitise cartilage mechanical response, deformation especially, to changes in superficial zone stiffness and thus sensitise the cartilage to further degenerative changes. This in turn offers a potential mechanistic-basis for the observation that mechanical parameters of cartilage for normal and osteoarthritic populations overlap extensively (Brown et al., 2007).

CRediT authorship contribution statement

Jonathan P. Whiteley: Visualization, Validation, Software, Project administration, Methodology, Investigation, Formal analysis, Data curation, Conceptualization, Writing – original draft, Writing – review & editing. **Cameron P. Brown:** Writing – review & editing, Methodology, Investigation, Conceptualization, Formal analysis. **Eamonn A. Gaffney:** Methodology, Investigation, Formal analysis, Conceptualization, Writing – original draft, Writing – review & editing.

Declaration of competing interest

The authors declare that they have no known competing financial interests or personal relationships that could have appeared to influence the work reported in this paper.

Data availability

Data will be made available on request.

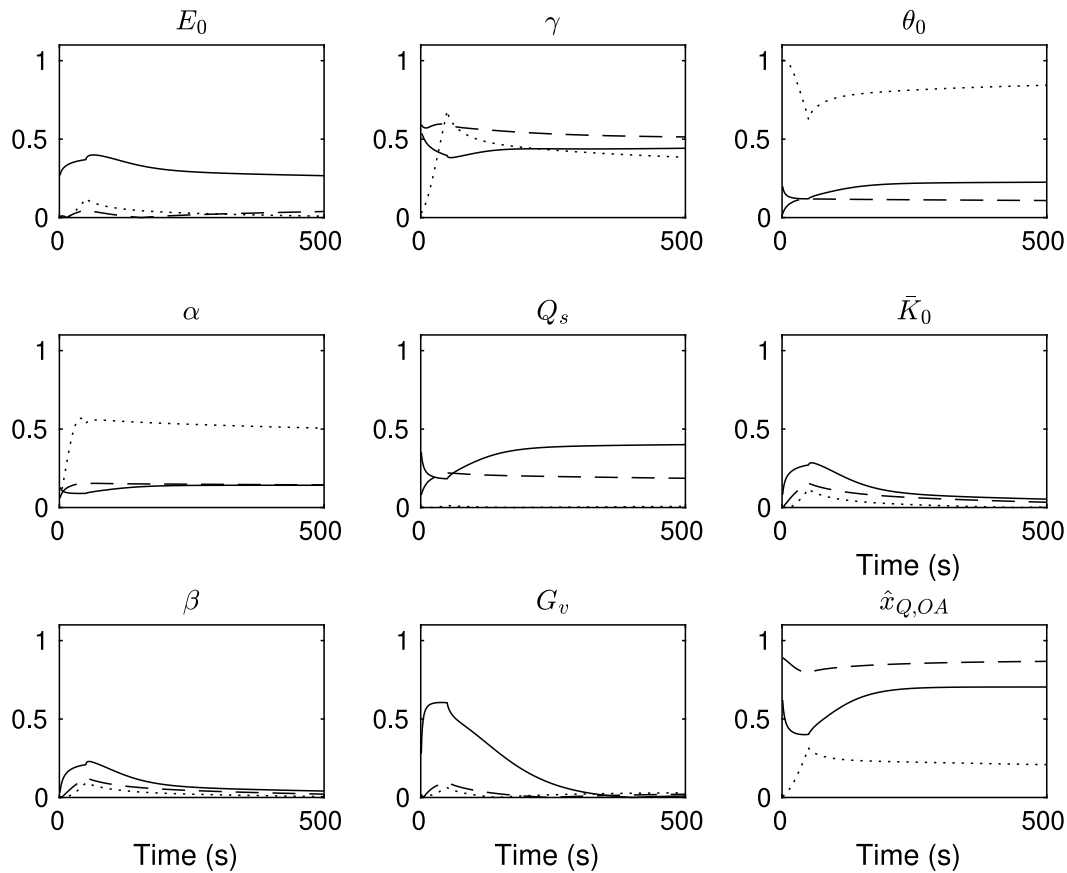


Fig. 11. PCA sensitivity indices as a function of time for simulations of osteoarthritic cartilage tissue where $\bar{K}_{OA} = 40\bar{K}_0$. The solid lines represent indices calculated using S_{tot} , broken lines indices calculated using the maximum strain, and dotted lines indices calculated using the minimum porosity.

Appendix. Properties of the calcified layer and the boundary conditions at the tidemark.

For the boundary conditions at the tidemark we consider the calcified cartilage to provide a fixed and impermeable boundary.

This boundary is treated as fixed since calcified cartilage is reported to be much stiffer than deep zone cartilage. Considering measurements for bovine patella cartilage, to match the cartilage used in the measurements of Young's modulus in Table 1, Mente and Lewis (1994) report sample ($n = 8$) minimum and mean calcified cartilage stiffnesses of $3 \times 10^7 \text{ N m}^{-2}$ and $1.6 \times 10^8 \text{ N m}^{-2}$ which, respectively, are one and two orders of magnitude greater than the deep zone Young's modulus in Table 1, with the latter based on measurements by Schinagl et al. (1997).¹ This much larger stiffness of the calcified layer entails much smaller deformation for the same loading, which we thus rationally approximate to be zero deformation, fixing the boundary.

We also consider the boundary to be impermeable. While it is extremely difficult to measure the permeability of the calcified cartilage directly, solute transport experiments such as those of Arkill and Winlove (2008) suggest substantially reduced permeability and porosity compared to that of uncalcified cartilage. Furthermore, fine scale computational models that also accommodate pore size and connectivity changes at the osteochondral interface by Pouran et al. (2021), using data from the scanning electron microscopy of human cadaver knee, indicate an enormous reduction in the permeability of calcified cartilage. This computational study indicates the permeability of calcified

cartilage is on the scale of $2 \times 10^{-23} \text{ m}^2$, while the scale of non-calcified cartilage permeability used in the manuscript is given by $\bar{K}_0 \eta \sim 2 \times 10^{-18} \text{ m}^2$ where $\eta \approx 10^{-3} \text{ N m}^{-2} \text{ s}$ is the interstitial fluid viscosity (taken to be that of water for order of magnitude estimation). This constitutes a drop in permeability by five orders of magnitude on passing into calcified cartilage through the tidemark, and thus we represent the calcified cartilage boundary as impermeable.

References

- Antons, J., Marascio, M.G., Nohava, J., Martin, R., Applegate, L.A., Bourban, P.E., Pioletti, D.P., 2018. Zone-dependent mechanical properties of human articular cartilage obtained by indentation measurements. *J. Mater. Sci., Mater. Med.* 29, 57.
- Arkill, K.P., Winlove, C.P., 2008. Solute transport in the deep and calcified zones of articular cartilage. *Osteoarthr. Cartil.* 16, 708–714.
- Ateshian, G.A., 2007. On the theory of reactive mixtures for modeling biological growth. *Biomech. Model Mechanobiol.* 6, 423–445.
- Athanasίου, K.A., Darling, E.M., Hu, J.C., DuRaine, G.D., Hari Reddi, A., 2013. *Articular Cartilage*. CRC Press.
- Benninghoff, A., 1925. Form und bau der Gelenknorpel in ihren Beziehungen zur Funktion. *Forschung* 2 (2), 783–825.
- Brown, C.P., Crawford, R.W., Oloyede, A., 2007. Indentation stiffness does not discriminate between normal and degraded articular cartilage. *Clin. Biomech.* 22 (7), 843–848.
- Buckwalter, J.A., Mow, V.C., Ratcliffe, A., 1994. Restoration of injured or degenerated articular cartilage. *JAAOS-J. Amer. Acad. Orthop. Surg.* 2 (4), 192–201.
- Chen, S.S., Falcovitz, Y.H., Schneiderman, R., Maroudas, A., Sah, R.L., 2001. Depth-dependent compressive properties of normal aged human femoral head articular cartilage: relationship to fixed charge density. *Osteoarthr. Cartil.* 9 (6), 561–569.
- Collins, D.H., 1939. The pathology of osteoarthritis. *Br. J. Rheumatol.* 1, 248–262.
- Collins, D.H., 1949. *Osteoarthritis. The Pathology of Articular and Spinal Disease*. Edward Arnold & Co, London, UK.
- DiSilvestro, M., Suh, J.-K.H., 2001. A cross-validation of the biphasic poroviscoelastic model of articular cartilage in unconfined compression, indentation, and confined compression. *J. Biomech.* 34, 519–525.

¹ Schinagl et al. (1997) estimate the cartilage stiffness for the deepest 250 μm by regression from less deep cartilage, rather than direct measurement, and thus this estimate is not used to consider calcified cartilage stiffness.

- DiSilvestro, M., Zhu, Q., Wong, M., Jorvelin, J., Suh, J.-K.F., 2001. Biphasic poroviscoelastic simulation of the unconfined compression of articular cartilage: I—simultaneous prediction of reaction force and lateral displacement. *J. Biomech. Eng.* 123, 191–197.
- Han, D., Wang, Z., Wang, Q., Wu, B., Yu, T., Wang, D., 2019. Analysis of the Kozeny-Carman model based on pore networks. *J. Geophys. Eng.* 16, 1191–1199.
- Hayami, T., Pickarski, M., Zhuo, Y., Wesolowski, G.A., Rodan, G.A., Duong, L.T., 2006. Characterization of articular cartilage and subchondral bone changes in the rat anterior cruciate ligament transection and meniscectomized models of osteoarthritis. *Bone* 38 (2), 234–243.
- Jolliffe, I.T., Cadima, J., 2016. Principal component analysis: a review and recent developments. *Phil. Trans. R. Soc. A* 374, 20150202.
- Klika, V., Gaffney, E.A., Chen, Y.-C., Brown, C.P., 2016. An overview of multiphase cartilage mechanical modelling and its role in understanding function and pathology. *J. Mech. Behav. Biomed. Mater.* 62, 139–157.
- Klika, V., Whiteley, J.P., Brown, C.P., Gaffney, E.A., 2019. The combined impact of tissue heterogeneity and fixed charge for models of cartilage: the one-dimensional biphasic swelling model revisited. *Biomech. Model. Mechanobiol.* 18, 953–968.
- Kuyinu, E.L., Narayanan, G., Nair, L.S., Laurencin, C.T., 2016. Animal models of osteoarthritis: classification, update, and measurement of outcomes. *J. Orthop. Surg. Res.* 11, <http://dx.doi.org/10.1186/s13018-016-0346-5>.
- Lai, W.M., Hou, J.S., Mow, V.C., 1991. A triphasic theory for the swelling and deformation behaviors of articular cartilage. *J. Biomech. Eng.* 113, 245–258.
- Mankin, H.J., Dorfman, H., Lippiello, L., Zarins, A., 1971. Biochemical and metabolic abnormalities in articular cartilage from osteoarthritic human hips. II. Correlation of morphology with biochemical and metabolic data. *The Journal of Bone and Joint Surgery* 53A, 523–537.
- Marino, S., Hogue, I.B., Ray, C.J., Kirschner, D.E., 2008. A methodology for performing global uncertainty and sensitivity analysis in systems biology. *J. Theoret. Biol.* 254, 178–196.
- Maroudas, A., 1968. Physicochemical properties of cartilage in the light of ion exchange theory. *Biophys. J.* 8, 575–595.
- Maroudas, A., Bullough, P., 1968. In vitro degradation of articular cartilage: does trypsin treatment produce consistent results? *Nature* 219, 1260–1261.
- Mente, P.L., Lewis, J.L., 1994. Elastic modulus of calcified cartilage is an order of magnitude less than that of subchondral bone. *J. Orthop. Res.* 12, 637–647.
- Mohammadi, H., Mequanint, K., Herzog, W., 2013. Computational aspects in mechanical modeling of the articular cartilage tissue. *Proc. Inst. Mech. Eng. H-J. Eng. Med.* 227 (H4), 402–420.
- Moody, H.R., Brown, C.P., Bowden, J.C., Crawford, R.W., McElwain, D.L.S., Oloyede, A., 2006. In vitro degradation of articular cartilage: does trypsin treatment produce consistent results? *J. Anat.* 209 (2), 259–267.
- Mow, V.C., Ratcliffe, A., Poole, A.R., 1992. Cartilage and diarthroidal joints as paradigms for hierarchical materials and structures. *Biomaterials* 13, 67–97.
- Nieminen, M.T., Rieppo, J., Silvennoinen, J., Toyras, J., Hakumaki, J.M., Hyttinen, M.M., Helminen, H.J., Jurvelin, J.S., 2002. Spatial assessment of articular cartilage proteoglycans with Gd-DTPA-Enhanced T1 imaging. *Magnetic Resonance in Imaging* 48 (4), 640–648.
- Pauli, C., Whiteside, R., Heras, F.L., Nesic, D., Koziol, J., Grogan, S.P., Matyas, J., Pritzker, K.P., D'Lima, D.D., Lotz, M.K., 2012. Comparison of cartilage histopathology assessment systems on human knee joints at all stages of osteoarthritis development. *Osteoarthr. Cartil.* 20, 476–486.
- Pierce, D.M., 2022. Multi-phase, large-strain constitutive models of cartilage for finite element analyses in 3-D. *Arch. Appl. Mech.* 92 (2, SI), 513–528. <http://dx.doi.org/10.1007/s00419-021-01959-5>.
- Pouran, B., Raoof, A., de Winter, D.A.M., Arbabi, V., Bleys, R.L.A.W., Beekman, F.J., Zadpoor, A.A., Malda, J., Weinans, H., 2021. Topographic features of nano-pores within the osteochondral interface and their effects on transport properties – a 3D imaging and modeling study. *J. Biomech.* 123, 110504.
- Radin, E.L., Rose, R.M., 1986. Role of subchondral bone in the initiation and progression of cartilage damage. *Clin. Orthop. Rel. Res.* (213), 34–40.
- Renardy, M., Joslyn, L.R., Millar, J.A., Kirschner, D.E., 2021. To Sobol or not to Sobol? The Effects of sampling schemes in systems biology applications. *Math. Biosci.* 337, <http://dx.doi.org/10.1016/j.mbs.2021.108593>.
- Saarakkala, S., Julkunen, P., Kiviranta, P., Makitalo, J., Jurvelin, J.S., Korhonen, R.K., 2010. Depth-wise progression of osteoarthritis in human articular cartilage: investigation of composition, structure and biomechanics. *Osteoarthr. Collagen* 18 (1), 73–81.
- Saltelli, A., Tarantola, S., Chan, K.P.-S., 1999. A quantitative model-independent method for global sensitivity analysis for model output. *Technometrics* 41, 39–56.
- Schaibly, J.H., Shuler, K.E., 1973. Study of the sensitivity of coupled reaction systems to uncertainties in rate coefficients. II applications. *J. Chem. Phys.* 59, 3879–3888.
- Schinagl, R.M., Gurskis, D., Chen, A.C., Sah, R.L., 1997. Depth-dependent confined compression modulus of full-thickness bovine articular cartilage. *J. Orthop. Res.* 15, 499–506, First published online Feb 2005, <https://onlinelibrary.wiley.com/doi/10.1002/jor.1004>.
- Setton, L.A., W., Z., Mow, V.C., 1993. The biphasic poroviscoelastic behavior of articular cartilage: Role of the surface zone in governing the compressive behavior. *J. Biomech.* 26, 581–592.
- Whiteley, J.P., Gaffney, E.A., 2020. Modelling the inclusion of swelling pressure in a tissue level poroviscoelastic model of cartilage deformation. *Math. Med. Biol.* 37, 390–429.
- Wilson, W., Huyghe, J.M., van Donkelaar, C.C., 2006. A composition-based cartilage model for the assessment of compositional changes during cartilage damage and adaptation. *OsteoArthr. Cartil.* 14, 554–560.
- Wilson, W., Huyghe, J.M., van Donkelaar, C.C., 2007. Depth-dependent compressive equilibrium properties of articular cartilage explained by its compression. *Biomech. Model. Mechanobiol.* 6, 43–53.